Sedimentation and flow through porous media: Simulating dynamically coupled discrete and continuum phases

Stefan Schwarzer*
Laboratoire de Physique Mécanique des Milieux Hétérogènes, Ecole Supérieure de Physique et Chimie Industrielles, 75231 Paris, Cedex 05, France
and Höchstleistungsrechenzentrum, Forschungszentrum Jülich, 52425 Jülich, Germany
(Received 15 March 1995; revised manuscript received 5 September 1995)

We describe a method to address efficiently problems of two-phase flow in the regime of low but non-zero particle Reynolds number and negligible Brownian motion. One of the phases is an incompressible continuous fluid and the other a discrete particulate phase which we simulate by following the motion of single particles. Interactions between the phases are taken into account using locally defined drag forces. We apply our method to the problem of flow through random media at high porosity where we find good agreement to theoretical expectations for the functional dependence of the pressure drop on the solid volume fraction. We undertake further validations on systems undergoing gravity induced sedimentation. In this context we address the effects of modeling assumptions.

PACS number(s): 47.55.Mh, 47.55.Kf

I. INTRODUCTION

A classical problem of chemical engineering is the understanding of particulate two-phase flows, in which a continuous fluid constitutes one component and a discrete particle phase the other. The practical importance of understanding such a particle-laden flow is evidenced by its central role in geophysical phenomena like sand storms, dune formation, or sediment transport, by the importance of biological questions like the understanding of the flow properties of blood, or cell component separation techniques as ultracentrifugation, by industrial applications as diverse as pneumatic transport in tubes, catalytic cracking, biological and chemical reactors, solid fuel rocket motors, fluidized beds, sedimentation, filtration, and many more [1,2].

If the discreteness of the particulate phase is fully taken into account then the mathematical formulation of the flow problem involves (i) a field equation for the continuous fluid phase — in most cases the Navier-Stokes equation, subject to a set of boundary conditions both on the container walls and the surfaces of the suspended particles — and (ii) a set of differential equations for the time evolution of the degrees of freedom of the individual constituents of the particulate phase. Due to the extremely complicated boundary conditions and the nonlinearity of the underlying equations, an analytical solution to this problem is impossible, except for exceptionally simple cases. A numerical treatment, however, even with simplifying assumptions, still poses tremendous practical problems.

Several simulation techniques have been developed which we briefly review here. (a) Finite volume techniques [3] that implement no-slip boundary conditions on the surface of each particle have been employed for very few particles. The treated Reynolds numbers are, in principle, only limited by the grid resolution and the computation time available. Similarly, (b) lattice Boltzmann techniques for the fluid equation have been used to simulate up to 1024 suspended particles [4]. So far, these have come closest to providing realistic simulations of two-phase flows with many particles. Most other approaches involve certain assumptions that are only true in limited parameter ranges: One important class of algorithms uses the Stokesian dynamics technique [5,6] valid for low Reynolds number flow to (c) obtain the flow field consistent with no-slip boundary conditions [7] or (d) approximate the particles as being pointlike [8,9]. Groups of point forces [10] have been used to approximate particles of finite extension in low Reynolds number flow.

(e) More popular in the engineering sciences, but less rigorous are continuum approximations that involve two sets of continuum equations, one for the fluid phase and one for the particulate phase. The boundary conditions on the particle surface and their influence on the flow is then represented by local drag forces depending on the solid volume fraction and local velocity differences [11,12]. In these approaches there remain open questions in the determination of the proper constitutive equation for the solid and the momentum exchange between the phases.

(f) To circumvent some of these latter problems of the pure continuum approaches, algorithms have come into fashion that combine a discrete element [13] or molecular-dynamics description [14] of the particles with a continuum equation for the fluid as in (a), but use a drag term to couple the two phases as in the pure continuum formulations (e) [15,16].

In this paper we will describe an algorithm of type (f). Such a method allows immediate access to basically all physically relevant quantities in the system, including particle coordinates and both particle and fluid velocities,

* Electronic address: stefan@pmmh.espci.fr

at computational costs comparable to a "standard" real-space Navier-Stokes integration. The main drawback is that a neglect of the proper boundary conditions in the treatment of the fluid will result in an inaccurate rendering of the short-scale flow properties. Since, however, our main focus will be the ability of the algorithm to describe collective phenomena, i.e., the effects that arise when the number of particles is large, we do not have the ambition to describe accurately the local flow fields on the scale of the particle size. At the moment the detailed effects of neglecting certain aspects of the local flow are not clear to us. It seems that an answer to this question is intertwined with the question of the existence of hydrodynamic screening in the studied systems, a phenomenon that is still under active investigation [17–19].

It is our goal to see which and how collective phenomena emerge directly from simple modeling assumptions — as opposed to using semiempirical expressions as, e.g., done in Refs. [15,16]. In particular, we rely on the fact that the long-range hydrodynamic interactions, which we presume to be the most important for collective phenomena, are correctly represented by the velocity and pressure fields according to the Navier-Stokes integration under consideration of an additional field representing the particle density.

The purpose of this paper is to give a detailed description of the simulation algorithm that we use to model particulate two-phase flow and its validation and assessment in the cases of (i) flow through a "porous medium" consisting of the "particles" in the simulation that are kept at fixed positions and (ii) of particles that undergo sedimentation in a suspension under the influence of gravity. In Sec. II we will first describe a two-dimensional (2D) implementation of the algorithm. Then, in Sec. III, we discuss first the case of flow through a porous medium (Sec. III A) and second the case of sedimenting particles (Sec. III B). A dimensionless form of the studied equations is given in the Appendix.

II. THE ALGORITHM

We aim at a simulation of macroscopic, hard sphere particles that interact on contact when the interstitial fluid plays no important role. In addition, they interact over long-range hydrodynamic forces, mediated by an incompressible fluid medium between the particles. For the moment, we consider a 2D implementation of our project. Since the analytic aspects of the solution of the Navier-Stokes equation in two dimensions are very different from the three-dimensional (3D) solution, we expect at best a qualitative agreement to the features of real 3D flows. However, we feel justified to study the 2D problem if it is possible to find qualitative knowledge on that way.

We organize the description of our algorithm into three main parts. In the first section we describe details of the employed molecular-dynamics technique for the particulate phase. The second compiles the fundamental equations for the fluid phase and the details of their solution. In the third section we elaborate on the particle-fluid interaction.

A. Molecular dynamics of the particle phase

1. Single particle properties and forces

Each particle i in the simulation is characterized by its radius r_i. We take the particle size distribution to be slightly polydisperse with the radii r_i drawn from a Gaussian distribution $h_p(r/\bar{r})$ with mean $\bar{r}$, which is cut off at its standard deviation $p\bar{r}$,

$$h_p(r/\bar{r}) \propto \begin{cases} \exp\left[-\frac{1}{2}\frac{(r/\bar{r}-1)^2}{p^2}\right], & \text{if } |r/\bar{r}-1| < p, \\ 0, & \text{otherwise.} \end{cases} \quad (1)$$

Here, the distribution is written in terms of the dimensionless radius $r/\bar{r}$ and the polydispersity parameter p.

We disregard effects of rotational motion of the particles and only consider their translation. As justification for this approximation we note that translational-rotational coupling is generally weak, except maybe in the high-density limit [20]. Thus we describe the particle motion only by the coordinates of their center of mass $\vec{x}_i = (x_i, y_i)$. Although the particle centers are constrained to lie in the x-y plane, we will assume — for reasons that we address in Sec. II C — that the particles can otherwise be regarded as three dimensional. Therefore we associate with each particle a mass $m_i = (4/3)\pi r_i^3 \rho_p$, where ρ_p is the constant particle density.

We consider the following forces to be acting on particle i:

$$\vec{F}_i = \frac{4}{3}\pi r_i^3(\rho_p - \rho_l)\vec{g} + \vec{F}_i^w + \vec{F}_i^d + \sum_j (\vec{F}_{ij}^n + \vec{F}_{ij}^t). \quad (2)$$

Here, $\vec{F}_i$ is the sum of all forces on i, the $\vec{F}_i^w$ are forces due to the presence of the boundary, the term proportional to gravity $\vec{g}$ accounts for particle weight and buoyancy. The drag force $\vec{F}_i^d$ will be discussed in Sec. II C. The sum runs over the other particles in the system, but is effectively restricted to the neighborhood of particle i, since we will only introduce short-range interparticle forces in the radial ($\vec{F}_{ij}^n$) and the tangential ($\vec{F}_{ij}^t$) direction in the next two sections.

Container walls, if present, manifest themselves by elastic forces and frictional forces in analogy to those acting between two particles. We will use for them the equations that result from those for two collision partners — to be introduced below — in the limit of the other particle having infinite mass and radius. In the direction of $\vec{g}$, we account for the weight of the particles. Acting opposite to gravity, we add the buoyancy reaction of the fluid, which equals the weight of the displaced fluid of constant density ρ_l. Our coordinate system is chosen such that $\vec{g}$ points in the $-y$ direction.

The forces from Eq. (2) enter the equations of motion for the particulate phase, $m_i\ddot{\vec{x}}_i = \vec{F}_i$. We solve this coupled system employing a fourth-order Gear predictor-corrector algorithm as described, e.g., in [14].

2. Pairwise interparticle forces in the radial direction

At very low Reynolds numbers the lubrication forces between particles play an important role. Since they have

a divergent character when the particles come close, particles in principle do not touch in this regime. However, if the mean free path of the fluid molecules comes into the order of the particle spacings in the system, if the particle based Reynolds numbers are no longer small, or if the particles are assumed to have some surface roughness, then they will touch and we cannot avoid modeling the contact forces between them.

If no fluid is present, then the particles are force free until they touch, whereupon strong repulsive and dissipative forces act between them, resulting from the viscoelastic properties of the particles. To model these forces, we use here contact models frequently employed in granular matter research [13,21,22]. The first of the forces acting on member i of a particle pair i,j in contact is an elastic restoring force $\vec{F}_{ij}^{\rm el}$. This force is proportional to the *virtual overlap* $\xi_{ij} \equiv (r_i + r_j) - |\vec{x}_i - \vec{x}_j|$ of the particles. If the overlap is positive, then

$$\vec{F}_{ij}^{\rm el} = -k_n \xi_{ij} \vec{n}_{ij}, \quad \text{for } \xi_{ij} > 0. \tag{3}$$

Here, $\vec{n}_{ij} = (\vec{x}_j - \vec{x}_i)/|\vec{x}_j - \vec{x}_i|$ denotes the unit vector pointing from the center of particle i to the center of particle j and k_n is the stiffness of the contact, which we assume to be constant. [The determination of k_n for realistic contacts in 3D is not a trivial matter. The value of k depends on the exact physical processes governing the contact and thus in general on both material constants as the Young modulus E_p or the Poisson number σ_p and the geometry of the particles. In contrast to our assumption of a linear contact law in 2D, many researchers use the nonlinear Hertzian contact theory, in which $\vec{F}_{ij}^{\rm el} = -k_n \xi_{ij}^{3/2} \vec{n}_{ij}$. For equal sized spheres, the Hertzian theory gives $k_n = \sqrt{2r} E_p / 3(1-\sigma_p^2)$. We refer the reader to the Tables I and II for parameter values in our simulations.] As mentioned above, the force vanishes if the particles do not overlap, i.e., $\xi_{ij} < 0$.

To take the dissipative character of the contact into account, we add a velocity-dependent friction term to the elastic restoring force. This damping force shall also act in the direction of the line connecting the particle centers (the *normal* direction) and be proportional to the normal relative particle velocity. On inclusion of this term, we obtain for the contact force $\vec{F}_{ij}^{c,n}$ in the normal direction

TABLE I. List of parameters for the simulation of flow through porous media. Deviating parameters are stated in the text. In particular, the Reynolds number Re varies.

L_x/L_y	Aspect ratio	1/2
$L_x/\bar{r}$	System height	200
$z/\bar{r}$	Stokes force reference length	2
$\Delta x/\bar{r}$	Grid resolution	2.5
p	Polydispersity	0.1

$$\vec{F}_{ij}^{c,n} = [-k_n \xi_{ij} - 2\gamma_n m_{\rm red} (\dot{\vec{x}}_j - \dot{\vec{x}}_i) \cdot \vec{n}_{ij}] \vec{n}_{ij}. \tag{4}$$

In this relation, $m_{\rm red}$ is the reduced mass $m_i m_j/(m_i + m_j)$ of the pair in contact and γ_n determines the strength of the dissipation. We have suppressed the indices on $m_{\rm red}$ and γ_n, but we consider them to vary among different particle pairs.

Equation (4) is the equation for a damped harmonic oscillator while the particles are in contact. For a given initial normal relative particle velocity $\vec{v}_i^n$ it can be solved analytically for the velocity after the contact $\vec{v}_f^n$. Since energy is dissipated, the ratio of these velocities is less than one; its value is termed *restitution coefficient* $e \equiv |\vec{v}_f^n|/|\vec{v}_i^n|$. One obtains for a specific particle pair (pair indices suppressed),

$$e = \exp\left[-\pi \Big/ \sqrt{\frac{1}{\gamma_n^2} \frac{k_n}{m_{\rm red}} - 1}\right]. \tag{5}$$

However, in the presence of a fluid at low Reynolds numbers, the dominant force at small distances between pairs of particles is the lubrication force $\vec{F}^l$ arising from the pressure necessary to replace the fluid within the gap between the two approaching spheres. The lubrication force damps the relative motion of the particles very strongly and diverges when the particles touch. Since in our approximate treatment of the fluid flow in particular the lubrication force is not well represented, we add it as an additional component of the particle-particle interactions, only active at short distances between the particles. The normal component of the lubrication force is [23]

TABLE II. List of parameters for the simulation of batch settling sedimentation. Deviating or varying parameters are stated in the text.

	L_x/L_y	Aspect ratio	1/2
	$L_x/\bar{r}$	System height	100
	$z/\bar{r}$	Stokes force reference length	2
	$\Delta x/\bar{r}$	Grid resolution	2.5
	p	Polydispersity	0.01
Re	$\bar{r} V_S \rho_l/\eta$	Particle Reynolds number	3.26×10^{-2}
St	$\bar{m} V_S/6\pi\eta\bar{r}^2 = (2/9)\mathrm{Re}\,\rho_p/\rho_l$	Average Stokes number	1.83×10^{-2}
Fr	$\bar{r} g/V_S^2$	Froude number	90.3
k_n^*	$k_n/6\pi\eta V_S$	Dimensionless spring constant	6.36×10^3
γ_n^*	$(1/4)[1/\delta - 1/(\delta+1)]$	Normal dissipation constant	4.5
	μ	Coulomb friction factor	0.3
γ_t^*	$\gamma_t m_{\rm red}/6\pi\eta\bar{r}$	Tangential damping	5.60×10^{-3}

$$\vec{F}_{ij}^{l,n} = -6\pi\eta \frac{r_{\rm red}^2}{(-\xi_{ij})}[(\dot{\vec{x}}_i - \dot{\vec{x}}_j)\cdot\vec{n}_{ij}]\vec{n}_{ij}. \quad (6)$$

In the above equation, η denotes the shear viscosity of the fluid and $r_{\rm red}$ the reduced radius $r_i r_j/(r_i + r_j)$ of the pair. Again we have suppressed the indices i and j for simplicity. The expression (6) is only valid for small positive separations between the surfaces of the two particles involved. These are reflected in negative overlaps ξ_{ij} of small modulus.

To take into account the limited range of validity of Eq. (6), we cut off $\vec{F}_{ij}^{l,n}$ where $(-\xi_{ij}) > r_{\rm red}$. To avoid a discontinuity in the force law, we subtract in Eq. (6) a constant equal to the value of the force just at this cutoff distance.

Furthermore, we remove the divergence at $\xi_{ij} = 0$ by adding to the value of $(-\xi_{ij})$ in the denominator a small positive number $\delta r^{\rm red}$. We have used a value of $\delta = 0.1$. Other than just being a numerical contrivance our physical motivation is found in the unavoidable surface roughness of particles in reality, which may cause the particle to come into contact despite the lubrication force.

Similarly, some contacts due to numerical inaccuracies are almost unavoidable in a dense system with many particles. To cover these spurious cases as graceful as possible, we have matched the γ_n of Eq. (4) such that the force law is continuous when $\xi = 0$. We obtain

$$2\gamma_n = 6\pi\eta \frac{r_{\rm red}}{m_{\rm red}}\left(\frac{1}{\delta} - \frac{1}{1+\delta}\right). \quad (7)$$

The verbal statements in the preceding three paragraphs condense into the following equations for the total interparticle forces in the normal direction, comprising both contact and lubrication forces,

$$\vec{F}_{ij}^{n} = \vec{F}_{ij}^{c,n} + \vec{F}_{ij}^{l,n} = \begin{cases} \vec{0}, & \text{if } (-\xi_{ij}) > r_{\rm red}, \\ [-6\pi\eta r_{\rm red}^2(\dot{\vec{x}}_j - \dot{\vec{x}}_i)\cdot\vec{n}_{ij}]\left[\dfrac{1}{-\xi_{ij}+\delta r_{\rm red}} - \dfrac{1}{(1+\delta)r_{\rm red}}\right]\vec{n}_{ij}, & \text{if } 0 < (-\xi_{ij}) < r_{\rm red}, \\ [-k_n\xi_{ij} - 2\gamma_n m_{\rm red}(\dot{\vec{x}}_j - \dot{\vec{x}}_i)\cdot\vec{n}_{ij}]\vec{n}_{ij}, & \text{if } \xi_{ij} > 0. \end{cases} \quad (8)$$

This force is continuous over the whole range of ξ_{ij}.

3. *Pairwise interparticle forces in tangential direction*

To model the frictional forces acting perpendicular to the line connecting the two particle centers — the *tangential* forces — we resort, as in the case of the normal forces, to notions of particle contact modeling. Here, the Coulomb law of sliding friction asserts that the magnitude of the tangential friction force $\vec{F}_{ij}^{t}$ is — on contact — proportional to the magnitude of the acting normal force $\vec{F}_{ij}^{n}$, [from Eq. (8)] with a constant of proportionality μ usually between 0.05 and 0.5,

$$|\vec{F}_{ij}^{t}| = \mu|\vec{F}_{ij}^{n}|. \quad (9)$$

This force is always directed opposite to the relative motion. Numerical problems may occur in near central impact, when the tangential component of the relative velocity is small, but $\vec{F}^n$ is large. Then the likewise large tangential component of the force resulting from (9) may cause an unphysical oscillatory behavior of the tangential velocity during contact. We therefore replace Eq. (9) for small relative tangential velocities with a velocity proportional friction term. Thus, finally, the tangential friction force on particle i becomes

$$\vec{F}_{ij}^{t} = -\min(\mu|\vec{F}_{i}^{n}|, 2\gamma_t m_{\rm red}|\vec{v}_{ij}^{t}|)\frac{\vec{v}_{ij}^{t}}{|\vec{v}_{ij}^{t}|}, \quad (10)$$

where $\vec{v}_{ij}^{t}$ has been introduced as an abbreviation for the relative tangential velocity $(\dot{\vec{x}}_i - \dot{\vec{x}}_j) - [(\dot{\vec{x}}_i - \dot{\vec{x}}_j)\cdot\vec{n}_{ij}]\vec{n}_{ij}$. For simplicity, we take γ_t to be constant.

We do not include shear contributions of the lubrication force into the interparticle forces, which is consistent with our neglect of the rotational degrees of freedom of the particles.

B. Fluid model

We describe the state of the fluid phase by three continuum fields, namely, (i) the velocity field $\vec{u}(\vec{x})$ of the fluid, (ii) its pressure $p(\vec{x})$, and (iii) a field $\epsilon(\vec{x})$ equal to the local volume fraction of fluid. These variables have physical meaning only as averages over volume on a scale larger than that of the individual particles. Their choice is motivated by continuum approaches to multiphase flow [11].

The position and geometry of the particles determine the field $\epsilon(\vec{x})$, which — for specific discrete tiling of the simulation plane — is a more or less a smooth function varying between 1 (no particles) and 0 (full occupation by particles), defined for all tiles and all times. Similarly, the time evolution of the velocity field $\vec{u}(\vec{x})$ is determined by the pressure distribution, viscous contributions, and a force distribution $\vec{f}(\vec{x})$ that comprises both volume forces on the fluid and momentum exchange contributions with the particulate phase (Sec. II C).

We follow Ref. [11] and write for the time evolution of the fluid velocity $\vec{u}$ (we will drop the argument $\vec{x}$ of the fields from here on),

$$\epsilon\rho_{\rm l}\left[\frac{\partial\vec{u}}{\partial t} + (\vec{u}\,\vec{\nabla})\vec{u}\right] = -\epsilon\vec{\nabla}p + \epsilon\eta\,\vec{\nabla}^2\vec{u} + \epsilon\vec{f}. \quad (11)$$

Although ϵ drops out of this equation, it enters into the momentum exchange contribution to $\vec{f}$, in the sense that the momentum transfer to the particulate phase due to the fluid phase — due to drag between particles and fluid — must be "fed back" to a fluid volume smaller than in the case without particles.

Since we have in mind applications to systems with typical velocities much smaller than the velocity of sound, we can assume that the fluid phase is incompressible. The equation of fluid mass continuity then reads

$$\frac{\partial \epsilon}{\partial t} + \vec{\nabla} \cdot (\epsilon \vec{u}) = 0. \tag{12}$$

Equation (12) presents a constraint on the velocity field that must be fulfilled at all times and may be employed to obtain the pressure field via an iterative procedure that we model after the artificial compressibility method of Chorin [24–26]. Here, we sketch the basic ideas of its 2D implementation briefly and refer the reader to the literature for more details.

We discretize the differential equations (11) and (12) in the following way. We place the velocity components u_x, u_y as well as the pressure p on three quadrilateral meshes with lattice spacing Δx. With respect to the pressure grid, the grids for the x and y velocity components are shifted by $\Delta x/2$ in the x and the y direction, respectively. This construction is commonly referred to as the MAC mesh and has several computational advantages. For instance, there is a simple means of avoiding numerical instabilities due to mesh decoupling [26]. The choice of location for the computational quantities is conceptually related to the location of variables in finite volume techniques for flux conservative differential equations, in which the fluxes are located on the corresponding faces of a control volume whereas the conserved quantities themselves reside in the center of the volume [27].

We obtain the pressure and the velocity components by an iterative procedure. Let the index n refer to values at time $t = t_n$ and $n+1$ to those at $t = t_{n+1} = t_n + \Delta t$ after a time step of duration Δt. The index k shall denote an iteration index. We define $p_{n+1,0} \equiv p_n$, i.e., we start an iteration for the new pressure at time t_{n+1} with the old values at t_n. We obtain a tentative velocity field at $t = t_{n+1}$ from an evaluation of the discretized Navier-Stokes equation (11),

$$\rho_l \frac{\vec{u}_{n+1,k+1} - \vec{u}_n}{\Delta t} = -\rho_l (\vec{u}_n \vec{\nabla}) \vec{u}_n - \vec{\nabla} p_{n+1,k} + \vec{f}_n + \eta \vec{\nabla}^2 \vec{u}_n. \tag{13}$$

where the symbol $\vec{\nabla}$ now denotes second-order precise difference operators on the lattice. As mentioned above, the solid volume fraction enters implicitly through $\vec{f}_n$. However, since (13) is a discretized Navier-Stokes equation, its stability criteria on the MAC grid have been studied and are reported, e.g., in [26,28]. These criteria state that the values Δx and Δt are subject to the two constraints

$$\Delta t \leq \frac{4\eta}{\rho_l (|u_x^{\max}| + |u_y^{\max}|)^2}, \tag{14}$$

and

$$\Delta t \leq \frac{\rho_l (\Delta x)^2}{4\eta}. \tag{15}$$

In general, the velocity field $\vec{u}_{n+1,k+1}$ resulting from (13) considered together with ϵ_n does not satisfy the continuity equation (12). Rather, one has to conceive the continuity equation as a constraint that determines the pressure field within the fluid such that the resulting velocity field satisfies the continuity equation at all times.

To this end, one derives an iterative procedure to determine an appropriate pressure field. This procedure is based on the idea that the local violation of the continuity equation, i.e., the value of the left-hand side of Eq. (12), can be used to correct the pressure field. The correction is taken in a direction such that the modulus of the violation is reduced in the next iteration step, after a new tentative velocity field has been determined. We write

$$p_{n+1,k+1} = p_{n+1,k} - \lambda \rho_l \left[\frac{\partial \epsilon_n}{\partial t} + \vec{\nabla} \cdot (\epsilon_n \vec{u}_{n+1,k+1}) \right]. \tag{16}$$

Here, a large value of the parameter λ is crucial for rapid convergence. The value of λ is, however, by stability requirements constrained to

$$0 < \lambda \leq \frac{(\Delta x)^2}{4\Delta t}. \tag{17}$$

In the simulations we have chosen λ to equal its upper stability limit.

It should be noted that the values ϵ_n in Eq. (16) are not all located on the same subgrid: the time derivative is taken at the pressure points and the ϵ_n multiplying $\vec{u}_{n+1,k+1}$ is realized by different fields, each living on the same subgrid as the associated velocity component. The values of ϵ_n are calculated at every time step using the instantaneous position of the particles and the location of the grid plaquettes. Similarly, the additional information contained in the particle velocities is employed to determine the necessary time derivative.

Once we have determined a new pressure field, we need to recalculate new velocity values consistent with the $p_{n+1,k+1}$. These velocities may be obtained using the Navier-Stokes equation (13), or equivalently, avoiding the costly reevaluation of Eq. (13), using the relation

$$\rho_l \frac{\vec{u}_{n+1,k+2} - \vec{u}_{n+1,k+1}}{\Delta t} = \vec{\nabla}(p_{n+1,k+1} - p_{n+1,k}). \tag{18}$$

The iteration of Eqs. (16) and (18) yields a new pressure field and after convergence a velocity field for time t_{n+1} such that the equation of continuity is satisfied.

For our purposes, the described algorithm has three advantages. (i) It generalizes straightforwardly to 3D and (ii) unlike spectral or stream-function methods it gives immediate access to the quantities p and $\vec{u}$ in real space. Fast access to the latter is crucial for the calculation of

the particle-fluid interaction. Moreover, (iii) only the chosen coarseness of the spatial and temporal discretization limits the range of Reynolds numbers addressable in the simulation. However, since the presence of the particles is communicated to the fluid among others through the field ϵ, it does not make much physical sense to use a computational grid on a scale smaller than the particle size.

For Reynolds numbers requiring such smaller grids, one could think of an approach to decompose the fluid equation into an equation for the average flow and additional equations describing the fluctuations around it, in the spirit of turbulence modeling [29].

C. Interaction of particles and fluid

The main problem in simulations of multiphase flow that tries to bypass the specification of boundary conditions on the phase boundaries is to specify an expression for the momentum exchange between fluid and particulate phase. Even for a single sphere this task is daunting [30]. For extended fixed random collections of spheres the phenomenological Ergun formula [31,32] gives the pressure gradient as a function of solid fraction and fluid velocity. Tsuji and co-workers [15,16] have used a "localized" form of the Ergun equation to estimate the force of the fluid on a sphere and obtain for pneumatic transport in pipes and fluidized beds qualitative agreement of flow patterns and quantitative agreement of some quantities.

Having the complicated situation in mind, and being aware of the significant approximation involved, we wish to explore the consequences of a very simple model for the momentum exchange. We use a local version of the "global" Stokes formula — which is just one term in the expression given by Maxey and Riley [30] for the drag on an isolated sphere under low-Reynolds-number conditions — to obtain the drag force acting on a sphere of radius r_i,

$$\vec{F}_i^d = -6\pi\eta r_i[\dot{\vec{x}}_i - \vec{u}(\vec{x}_i)]. \tag{19}$$

In order to evaluate the fluid velocity field at the location of the particle we interpolate linearly the velocity values from the closest four grid points. That is to say, if the pair (x, y) denotes the coordinates of one of these four "adjacent" grid points $\vec{x}_i$ then $w(x, y) \equiv (1-|x_i-x|/\Delta x)(1-|y_i-y|/\Delta x)$ is the weight associated with (x, y); the index i refers to the particle location. We obtain thus for some velocity component u the interpolated value $u(\vec{x}_i)$ as $u(\vec{x}_i) = \sum w(x, y)u(x, y)$. The sum extends over the four corners of the MAC grid plaquette associated with the component u into which $\vec{x}_i$ falls.

As Eq. (19) resembles the 3D expression for the drag on an isolated *sphere*, we should give here a motivation for this modeling assumption. A "pure" 2D simulation should, strictly speaking, be one of rigid, parallel *cylinders*. However, at a fixed small Reynolds number, the drag per unit length of a cylinder [33] does not depend on its radius. This behavior is very different from the observations in 3D experiments, where there is a strong dependence of the drag on the size of the spheres. Thus, in particular, effects of the particle polydispersity cannot be expected to be represented properly by a model based on drag forces of cylinders.

We therefore use Eq. (19) for the drag and refer the force (19) to a *reference length* z on the order of the average particle diameter. The picture behind this procedure that we have in mind is that we imagine the particle configuration repeating itself at all z length units submerged in a fluid infinitely extended in the z direction. However, both particles and fluid are constrained to move only in the x-y plane. The value of z is important when we calculate the drag per unit volume that enters into the Navier-Stokes equation and thus controls the degree of coupling between the two phases.

The finite drag force (19) acts on the fluid at the location of the center of the particle and we must thus — in order to convert it to the force density required in the continuum equation — represent it by a δ function at $\vec{x}_i$,

$$\vec{F}_i^d \frac{1}{z\epsilon(\vec{x})}\delta(\vec{x}-\vec{x}_i), \tag{20}$$

in the Navier-Stokes equation. The term $\epsilon(\vec{x})$ ensures that the force density refers to the fluid fraction alone, which is necessary to conserve momentum. We form the sum over all particles and add the uniform contribution of gravitation to obtain the full volume force density term,

$$\vec{f}(\vec{x}) = \rho_l\vec{g} + \sum_i \vec{F}_i^d \frac{1}{z\epsilon(\vec{x})}\delta(\vec{x}-\vec{x}_i). \tag{21}$$

On our computational lattice we implement the expression (21) by distributing $\vec{F}_i^d/z(\Delta x)^2\epsilon(\vec{x})$ to the four grid points closest to $\vec{x}_i$. To this end, we employ the same weights as already introduced above for the interpolation of the velocity components. For example, the contribution to point (x, y) is $(1-|x_i-x|/\Delta x)(1-|y_i-y|/\Delta x)\vec{F}_i^d/z(\Delta x)^2\epsilon(\vec{x})$. This concludes the description of the implementation of our algorithm.

We present a dimensionless form of the equations discussed in this section together with the values of parameters used in the simulation in the Appendix.

III. APPLICATION TO EXAMPLE PROBLEMS

We will now describe the results of the application of the described algorithm on selected physical problems in order to validate our approach, and assess its limitations or the consequences of using the simple drag law (19).

A. Flow through porous media

As our first system, we consider the motion of a fluid through a *fixed* random assembly of particles. Our mental picture is that the particle assembly is a model for a random porous medium with very high porosity. In the simulation, we then have to keep the particles pinned to

their initial positions. However, we calculate all forces acting between particles and fluid, but we only update the fluid's degrees of freedom in the computational time step. Excluded volume effects due the presence of the particle phase and local frictional drag still influence the fluid motion. Gravity is set to zero or, equivalently, the flow is considered to lie in the horizontal plane.

In the x direction the system has the width L_x and boundary conditions are periodic. We impose fixed superficial flow velocities u in the y direction at the inlet and outlet of the system at $y = 0$ and $y = L_y$, where L_y denotes the height of the system. A typical arrangement of particles in a small system of $L_x/\bar{r} \approx 33$ and $L_x/L_y = 0.5$ at Re $=3.75 \times 10^{-3}$ and the resulting stationary flow pattern is displayed in Fig. 1. The circles indicate the particles and the arrows indicate direction and magnitude of the fluid flux obtained by multiplying the local fluid volume fraction with the flow velocity. We see how the particle volume fraction influences the flow pattern such that the current concentrates in regions with few particles present. Note that the fluid velocity is defined everywhere in space, even at points covered by particles and that the flow velocities should therefore be considered as average values over the specific grid cell. Note also that the flux vectors are not displayed at their location used for computational purposes but are extrapolated to and displayed together with the color coded pressure at the location of the pressure points.

In this system, we measure the overall pressure drop per length $\Delta p/L_y$ as a function of the overall fluid volume fraction $\bar{\epsilon}$ of the medium and the superficial fluid velocity u. In the viscous regime the pressure drop is proportional to the fluid velocity u. We evidence a constant ratio of pressure drop to fluid velocity in Fig. 2 for several orders of magnitude of the particle Reynolds number Re $\equiv \rho_l \bar{r} u/\eta$ at fixed "porosity" $\bar{\epsilon}$.

We report our results in terms of the friction factor

$$f_p = -\bar{r}\Delta P/\rho_l u^2 L_y, \tag{22}$$

which is, due to the linearity of the pressure drop in the viscous regime, inversely proportional to the particle Reynolds number Re $\equiv \rho_l \bar{r} u/\eta$. Accordingly we have plotted in Fig. 3 the product f_p Re which — in the viscous regime — is independent of the Reynolds number. The product's value is plotted against the fluid volume fraction or porosity $\bar{\epsilon}$ based on the 3D volume of the particles divided by the box volume $L_x \times L_y \times z$, where z denotes the effective box depth introduced in Sec. II C. The three different curves in the plot indicated by symbols correspond to two different values of $z/\bar{r} = 2$ and $8/3$ and one run (lowest-lying curve) where only drag between particles and fluid has been considered in the simulation and the local fluid fraction $\epsilon(\vec{x})$ in Eqs. (11) and (12) has been kept equal to 1. The curves for different $z/\bar{r}$ collapse into a single universal curve. We consider this data collapse as an *a posteriori* justification of the picture of the simulated system that we have used to find a form for the momentum feedback to the fluid (Sec. II C).

Concerning the functional form of the result in 3D, the literature lists several phenomenological expressions for the porosity dependence of the friction factor [34]. Popular expressions for f_p Re include (i) the half-empirical Carman-Kozeny relation f_p Re $\sim (1-\bar{\epsilon})^2/\bar{\epsilon}^3$ and (ii) the phenomenological Rumpf-Gupte form f_p Re $\sim \bar{\epsilon}^{-5.5}$. Both relations are only valid in an intermediate range of porosity and do not apply to the limit of very high porosity or very low solid volume fraction. It follows from the results of, e.g., Brinkman [35] and Childress [36] that in this dilute limit and in 3D the lowest-order contributions yield

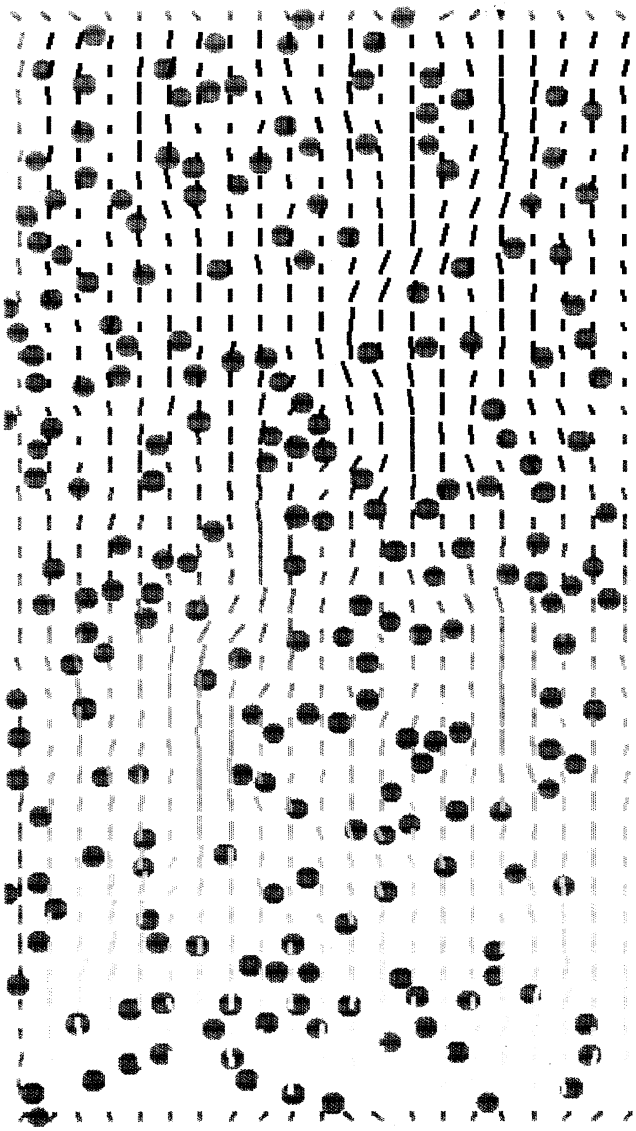

FIG. 1. 2D fluid flow pattern through a random assembly of "spheres." In this figure the 2D area fraction is $\bar{\epsilon} = 0.15$ and the particle-based Reynolds number Re $= 0.01$. Lines indicate the direction and the magnitude of the flow. Clearly visible are the effects of the mass conservation on the flow: The flow concentrates in regions with few particles and "engulfs" the particles on smaller scales.

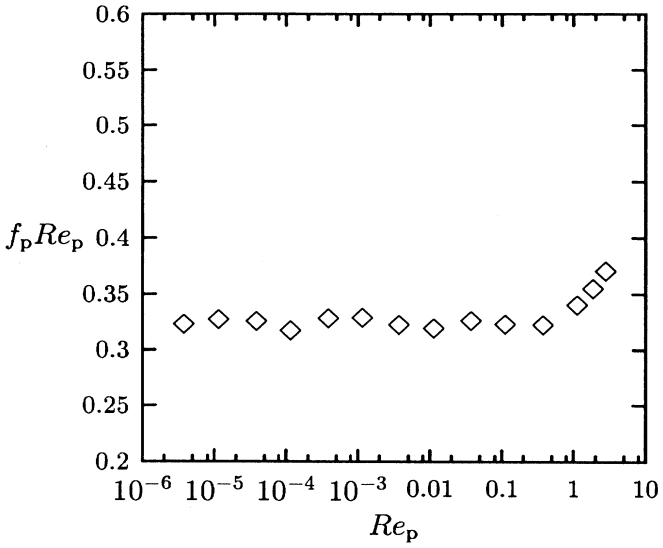

FIG. 2. We plot the product f_p Re of friction factor and particle Reynolds number vs the particle Reynolds number Re, at constant porosity $\bar{\epsilon} = 0.93$ $[= 1 - \sum_i (4/3)\pi r_i^3 / L_x L_y z]$. Apart from small statistical fluctuations due to different initial placements of the particles, the curve is constant in the regime of Reynolds numbers $\ll 1$, thus showing that the pressure drop is proportional to u as required by Darcy's law.

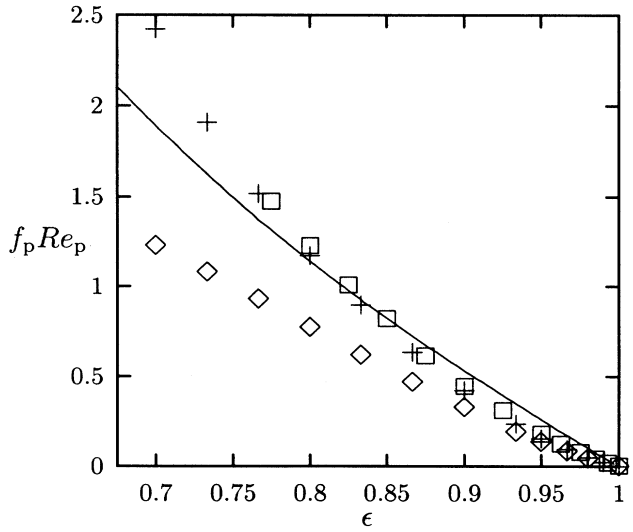

FIG. 3. We plot the product f_p Re of friction factor and particle Reynolds number vs the volume fraction $\bar{\epsilon}$. Different curves correspond to different flow rates (Reynolds numbers) and to different values of the system "depth" $z/\bar{r} = 2$ (+), $z/\bar{r} = 8/3$ (□). A third set of runs has been made for the case of only frictional coupling between fluid and obstacles, setting the fluid volume fraction to 1 everywhere (◇). The volume fraction $\bar{\epsilon}$ is calculated as 3D volume fraction, considering the particles as spheres and the simulation box as quadrilateral of extension $L_x \times L_y \times z$. For comparison we show relation (23) for the drag in a 3D dilute random bed of spheres.

$$f_p \,\mathrm{Re} = \frac{9}{2}(1-\bar{\epsilon})\left[1 + \frac{3}{\sqrt{2}}(1-\bar{\epsilon})^{1/2} + \frac{135}{64}(1-\bar{\epsilon})\ln(1-\bar{\epsilon})\right] \tag{23}$$

for the friction factor.

The solid line in Fig. 3 shows the prediction of the parameter free 3D formula (23). The simulated 2D friction factor as a function of increasing porosity vanishes faster than expected from (23). The lowest-lying "drag-only" curve in contrast is almost linear in $1 - \bar{\epsilon}$, as one would expect for the friction exercised by a cloud of pointlike obstacles on an otherwise unperturbed flow.

B. Sedimentation

We now discuss the application of our algorithm to the more general case when both particles and fluid are mobile and important dynamical consequences arise from the coupling of the two phases. A prototype example for this case is batch settling sedimentation. Imagine a homogeneous mixture of particles and fluid being placed into a quadrilateral — or for our purposes rectangular — container and being initially at rest. If there exists a density difference between particles and fluid, then gravitational driving forces will set the particles in motion. Complicated fluid-mediated hydrodynamic interactions between the particles lead to convoluted trajectories and give rise to collective phenomena as, for example, anisotropic self-diffusion of particles. The particles slowly settle to the bottom of the container with an average speed $\langle V(\Phi)\rangle$ that decreases as the volume fraction Φ of particles in the container increases. We have chosen here $\Phi \equiv 1 - \bar{\epsilon}$ to follow the convention in most of the literature on sedimentation. We display a typical situation during the batch settling process in Fig. 4.

The conditions of the simulation are periodic or no-slip boundary conditions in the horizontal x direction and no-slip boundary conditions in the vertical y direction. Gravity is taken to act in the $-y$ direction. One denotes as the hindered settling function $f_{\mathrm{hs}}(\Phi)$ the ratio of the sedimentation velocity $\langle V(\Phi)\rangle$ to the Stokes velocity V_S,

$$\langle V\rangle / V_S \equiv f_{\mathrm{hs}}(\Phi), \tag{24}$$

where

$$V_S = (2/9)(\rho_p - \rho_l) g \bar{r}^2 / \eta, \tag{25}$$

which is the settling velocity of an isolated sphere in an infinitely extended fluid.

We investigate $f_{\mathrm{hs}}(\Phi)$ for an almost monodisperse system. The particle Reynolds number $\mathrm{Re} = \rho_l \bar{r} V_S / \eta$ is smaller than 1, typically $\approx 3 \times 10^{-2}$ and (ii) the "simulation box" Reynolds number $\mathrm{Re}_b = \rho_l L_x V_S / \eta$ is 100 times larger, i.e., $\mathrm{Re}_b \approx 3$. Furthermore, we choose the particle size large enough such that the effects of Brownian motion may be neglected, corresponding to the regime

of high (iii) Peclet number. We have performed simulations and determined the settling velocity as a function of the solid fraction of the particle suspension. The following four different sets of conditions for "thought" experiments have been performed to assess the role and importance of lubrication and backflow for the simulations. In particular, the simulation series (i) includes lubrication effects [Eq. (6)], effects of particle void fraction [Eqs. (11) and (12)], and periodic boundary conditions in the x direction, perpendicular to gravity; (ii) differs from series (i) only in the respect that we have not considered the lubrication term (6). Without these lubrication forces, we choose the value of γ_n in Eq. (4) such that for pair collisions a restitution coefficient of 0.9 results [cf. Eq. (5)]; (iii) differs from (ii) in the respect that we have additionally set the fluid fraction $\epsilon(\vec{x})$ to 1, as if the particles consisted of fluid and not of a separate solid phase. The interaction of particle and fluid phase results only from the pointlike frictional drag between the two; (iv) differs from (i) only in the respect that we have used no-slip boundary conditions at $x = 0$ and $x = L_x$.

Figure 5 displays the hindered settling function of case (i). The "Stokes" velocity used to normalize the data has been obtained from simulations of single spheres. It

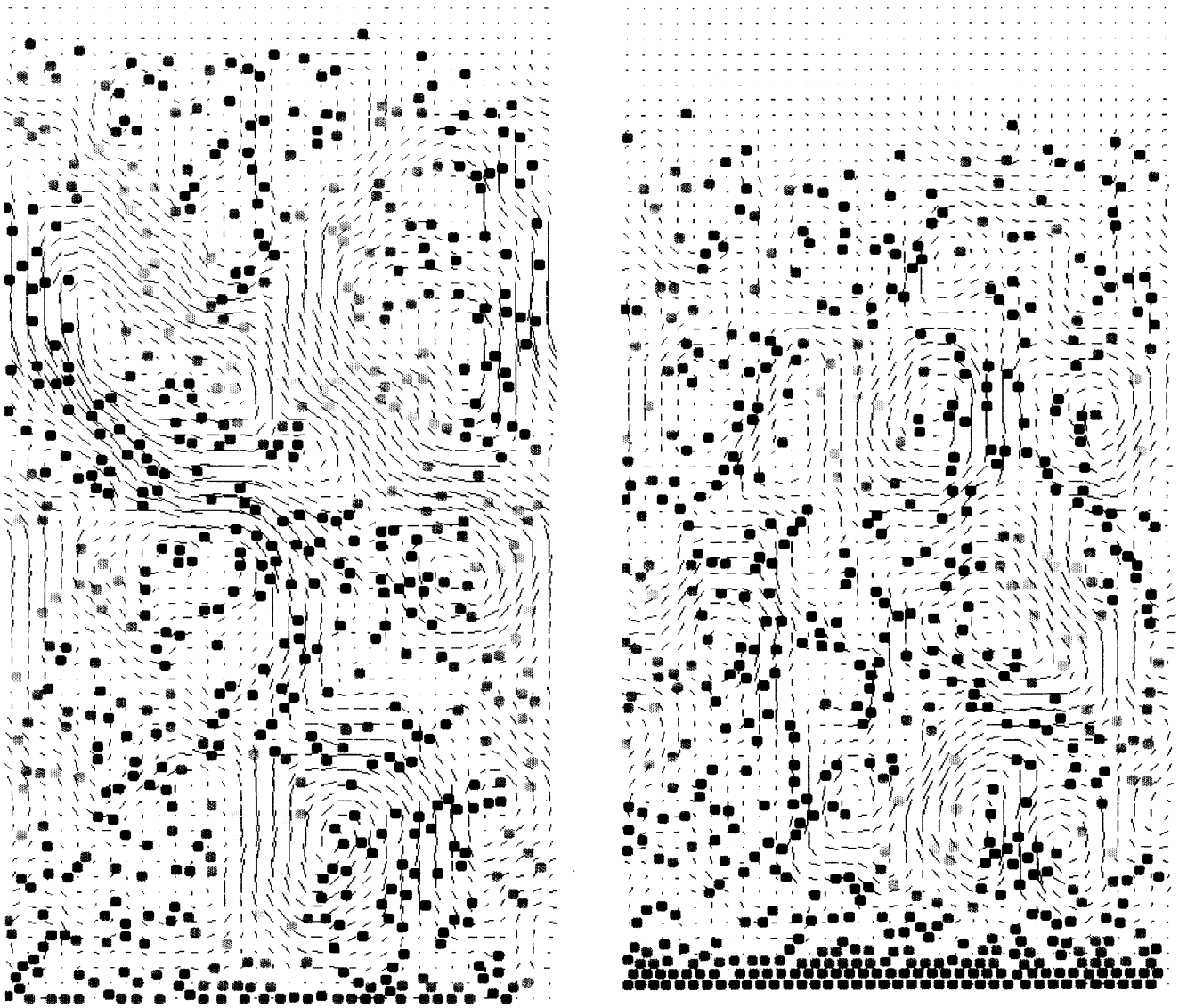

FIG. 4. Typical particle configurations during a batch settling simulation at $tV_S/\bar{r} =$ (a)5.2, (b) 16, (c) 26, (d) 36, (e) 46, and (f) 56 where t denotes time, V_S the Stokes velocity, and $\bar{r}$ the average particle radius. The system size is chosen to be comparatively small, $L_x/\bar{r} = 80$ and $L_y/L_x = 2$; 606 particles are visible and the 2D solid area fraction $\sum_i \pi r_i^2/L_xL_y$ is 0.10. Lines indicate the direction and amplitude of the fluid flow. Shades of gray denote the y component of the particle velocity, dark particles move down and light ones up. It is interesting to see that there is substantial internal motion of particles in complicated vortex patterns. The particle settling is visible "on average," for example, at the upper sedimentation front.

should be noted that (3D) experiments in the viscous regime — both Re_b and Re much smaller than 1 — often report a correlation with a $f_{\mathrm{hs}}(1-\Phi)^n$, $n \approx 5$ dependence [37,38], the Richardson-Zaki formula [39]. Our data, however, are characterized by an exponent $n \approx 3$ (solid line in Fig. 5). It is possible that in our case the larger value of Re_b prevents us from seeing $n \approx 5$. Of course, also the nature of hydrodynamic interactions in 2D — based on the behavior of the velocity disturbance introduced by a point force in Stokes flow — is quite different from the 3D case, such that probably only full 3D simulations can find $n = 5$ [40]. Firm analytical results for the sedimentation velocity are restricted to the dilute regime, where one finds corrections to the Stokes velocity that are linear in Φ [41,42], e.g.,

$$f_{\mathrm{hs}} = 1 - 6.55\Phi. \tag{26}$$

The graphs in Fig. 6 address the question of which way the resulting sedimentation velocities in series (ii) to (iv) differ from that in (i). To this end, we have calculated the ratios of the sedimentation velocities. First, the diamonds denote the ratio $\langle V^{(\mathrm{ii})}\rangle/\langle V^{(\mathrm{i})}\rangle$. Since lubrication alters the interactions between particles more significantly when the particle fraction is high, we see that the fraction deviates more and more from 1 as the solid fraction increases. The ratio becomes smaller than 1, which means that the system "without" lubrication sediments slower. We understand this behavior taking into account the strongly damping character of the lubrication force. Such damping forces between particles have the effect of reducing the *relative* velocity between them and thus favoring the creation of loosely connected particle agglomerates. These effects are well known for "dry" granular systems with dissipative contact interac-

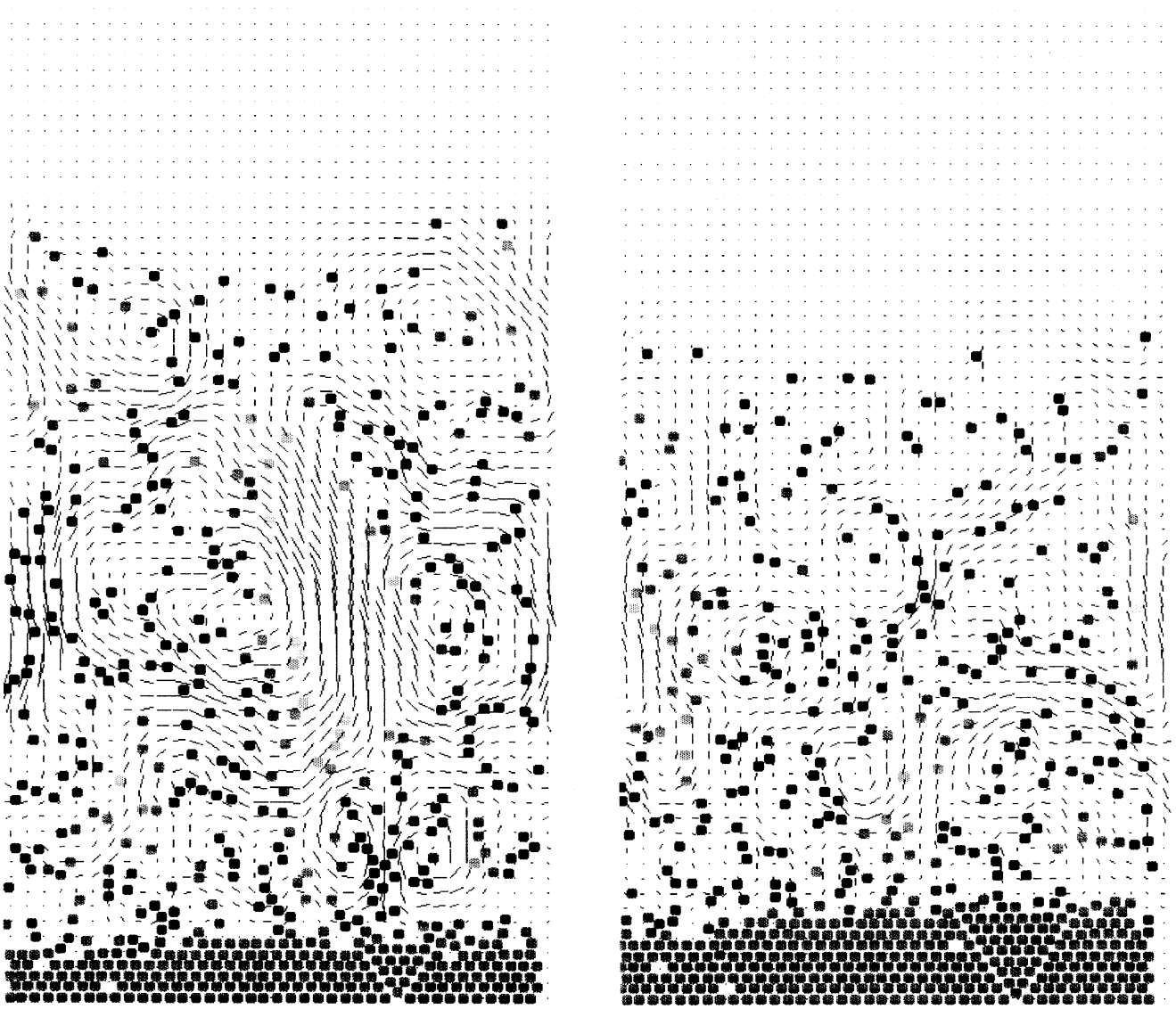

FIG. 4 *(Continued).*

tions between particle collisions [43,44]. These particle clusters then trap some fluid within and fall as almost coherent units. Such a unit displays a larger terminal fall velocity than its constituent particles alone since V_S is proportional to the squared radius of the falling object.

Second, we assess the effect of backflow in the simulation by setting $\epsilon(\vec{x}) = 1$ in the Navier-Stokes and the continuity equation [(11) and (12)]. The particles are then effectively pointlike as far as the fluid is concerned. Denoted by squares, the ratio $\langle V^{(\mathrm{iii})}\rangle/\langle V^{(\mathrm{ii})}\rangle$ starts at a value below 1 — which results from particularities in the momentum exchange modeling (see Sec. IV B) — and increases with volume fraction. We can estimate the effect of backflow by assuming that the average relative velocity of particles and fluid phase are the same in situations (ii) and (iii): A short calculation assuming that the average relative velocity between particles and fluid is the same in both cases predicts $\langle V^{(\mathrm{iii})}\rangle/\langle V^{(\mathrm{ii})}\rangle = 1/(1-\Phi) \approx 1+\Phi$. The observed increase is less steep as expected from this relation, indicating a more complicated effect as a consequence of the introduction of the volume fraction field, which we do not understand at this point.

Third, we have performed a simulation with no-slip boundary conditions on the container walls instead of the periodic boundary conditions used otherwise. We denote the data points for $\langle V^{(\mathrm{iv})}\rangle/\langle V^{(\mathrm{i})}\rangle$ by the diamonds. The ratio is, apart from a point at very low volume fraction, smaller than 1. The fluid velocity is constrained to be zero at the container walls and hence we believe that the motion of the fluid is altogether less vehement than in the periodic case. Since particle and fluid motion are very strongly coupled — the distance that a particle has to travel in order to reach a terminal velocity is much less than a particle diameter — the on average smaller

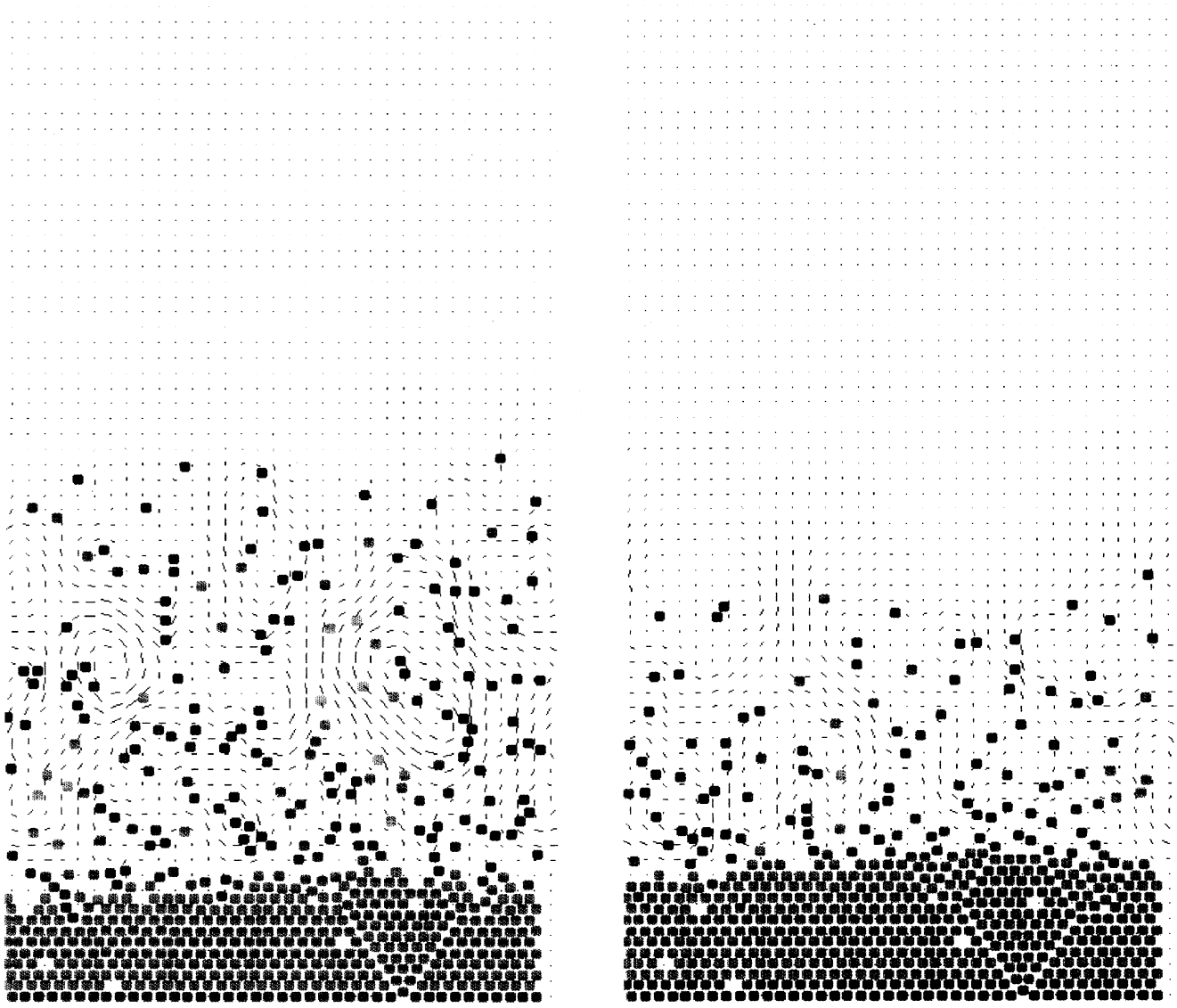

FIG. 4 *(Continued).*

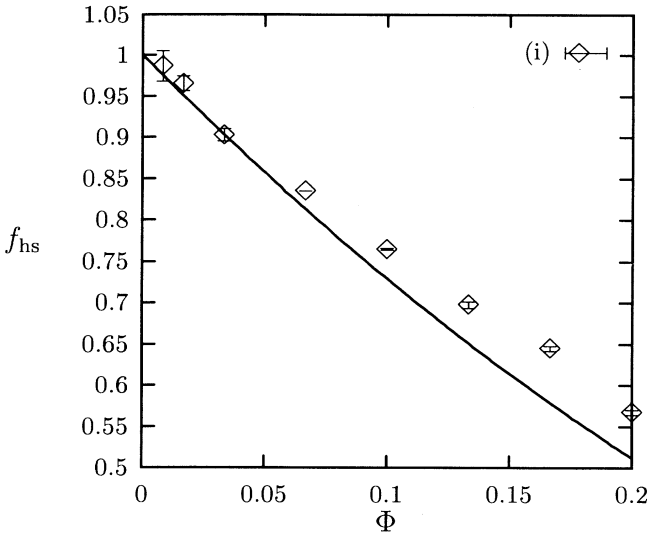

FIG. 5. Hindered settling function $f_{\rm hs} \equiv \langle V \rangle / V_S$ for simulation series (i) (see text), including lubrication, void fraction, and using periodic boundary conditions in the x direction. The ordinate shows the effective 3D solid fraction Φ, which is related to the 2D area fraction of particles in a simple way, given that the radius distribution of the particles is monodisperse: $\Phi = (4/3)(\bar{r}/z)\Phi_{\rm 2D}$. The data points have been averaged over three runs with different initial conditions. The solid line is the Richardson-Zaki relation $f_{\rm hs} = (1-\Phi)^n$ with an exponent $n = 3$, which significantly differs from the phenomenological 3D result $n \approx 5$.

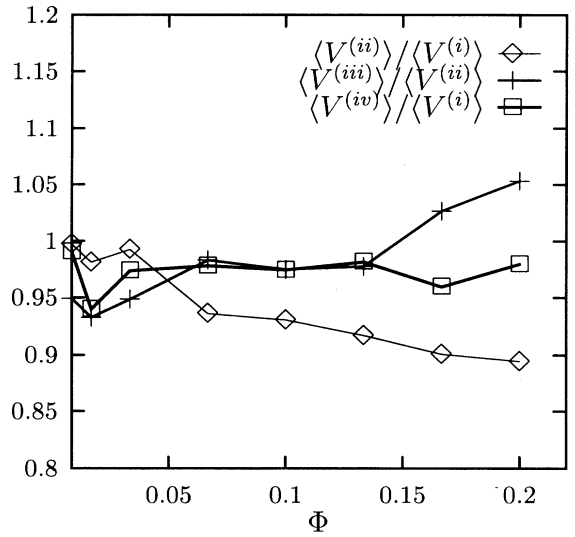

FIG. 6. Ratios of sedimentation velocities vs the effective 3D volume fraction Φ in the simulation computed under four different sets of simulation conditions (i)–(iv); for details see text. Diamonds denote the ratio the computed velocity disregarding lubrication (ii) to the velocity in the "full" simulation (i). Similarly, pluses denote the ratio of series (iii) to (ii) — no lubrication and in (iii) additionally the fluid fraction set to 1. Boxes denote the ratio (iv) to (i) for the difference between periodic and no-slip boundary conditions for the box walls. All data points have been computed using velocity averages over three runs with different initial conditions.

particle velocities at the container walls suffice to slow down the settling.

It should be mentioned here that Hinch has presented a unifying theoretical approach to both flow through random sphere assemblies and sedimentation that allows us to calculate expressions for the permeability and the average sedimentation speed in the dilute limit (see next paragraph) [45].

2D effects

We would also like to point out the fundamental differences in the nature of the long-range behavior of the velocity disturbances caused by a point (line) force in 2D low Reynolds number flow with logarithmic character $\sim \log(r)$ as compared to the disturbance due to a point force in 3D flow, which is $\sim 1/r$. Thus, it is not clear that theoretical or experimental results from 3D carry over or can be compared meaningfully with 2D results or simulations. In particular, one could expect that the logarithmic behavior in 2D leads to stronger velocity correlation effects than in 3D.

Under certain circumstances, for example, if the particle correlation function shows specific properties, the long-range part of the velocity disturbance may cancel, leading to hydrodynamic screening [19]. Its existence in 3D suspensions is disputed [17,18,46]. Due to the even stronger long-range effects in 2D, screening is probably absent in our sedimentation simulations.

IV. CONCLUSION AND OUTLOOK

A. General advantages of a drag-force based approach

The major advantage of a drag-force based algorithm as described here for the simulation of two-phase flows is the capability to simulate considerably large systems with relatively moderate computational requirements. At the same time one arrives without effort at a physical microscopic description of the particulate phase circumventing the problems of continuum approaches that have to specify the stress or the constitutive equation of the particulate phase. Such an algorithm is therefore a tool to obtain quick insight into collective effects of many particles. In fact, most of the known physical effects appear to be reproducible using only a very simple expression for the momentum exchange between phases.

In the present work, we have successfully reproduced the qualitative behavior of the mean sedimentation velocity on the particle solid fraction in non-Brownian suspensions and the volume fraction dependence of the friction factor in flow through porous media.

B. Specific problems of a drag-force based approach

We now list some of the problems that we have encountered performing the present study that will be addressed

in future research.

Let us first consider the behavior of a single particle in an otherwise resting fluid, both initially at rest. If the particle density is higher than the density of the fluid, the particle will experience a net force in the direction of gravity. As it falls, fluid will be dragged down with it in accordance with the momentum exchange rules and the requirements of the replacement of fluid as the local fluid fraction changes. As compared to the fluid velocity far away from the particle the local velocity is closer to the particle velocity. Consequently the isolated particle experiences a drag force that does not agree with the theoretical Stokes expression into which the particle velocity and the fluid velocity at infinity enter and the resulting terminal fall velocity of the particle is larger than the theoretical Stokes velocity. (This effect has been taken into account by using the measured terminal velocity of a single sphere in lieu of the theoretical Stokes velocity, for example, in the scaling of the mean sedimentation velocities to obtain the hindered settling function.)

One way to address this problem is to alter the drag law (19) by introducing a "drag coefficient" different from 6π and dependent on the, albeit unphysical, ratio of particle size to the grid spacing and physical parameters as the Reynolds number — this approach has been taken in [47]. However, the root of this problem lies in the treatment of the momentum exchange and indicates that a revision of its treatment is necessary.

One could imagine first that a better treatment of the momentum exchange should proceed along the lines of approximating the fluid stress tensor on the particle surface, which may be possible in the low-Reynolds-number regime. However, the principal limitation of our ansatz is that the flow velocities in the vicinity of the particle surface are not accurately rendered as required for an estimation of the stress on the particle, since we account for the flow only in an average sense.

Another possibility is to change the drag law. We have so far employed a simple Stokes expression. It is probably necessary to introduce a drag expression that additionally depends on the local particle density in addition to the local velocity difference between phases. We think that at least at high particle densities particle rotation also becomes important and must be included in the model. Moreover, we may have to use density-dependent local viscosities in the "Navier-Stokes" equation.

In conclusion, we should and will in the future use an improvement of our algorithm to tackle some of the problems listed above. However, even in the present state, we have a powerful tool at hand to assess cooperative effects of many-particle systems in which hydrodynamic interactions play an important role. We have successfully modeled flow around impurities at small and moderate volume fractions and found reasonable agreement in the case of a sedimenting system.

ACKNOWLEDGMENTS

I would like to acknowledge in particular long discussions with François Feuillebois, Hans Herrmann, Wolfgang Kalthoff, and Frank Tzschichholz and likewise encouraging and challenging conversations with D. Barnea, M. Fermigier, I. Goldhirsch, and E. Guazzelli. I am indebted to John Hinch for valuable insights concerning the problem of flow through random media as well as its relation to the sedimentation problem. The author thanks the scientific council of NATO for financial support (granted through the DAAD, Bonn).

APPENDIX: DIMENSIONLESS FORMULATION

In the preceding text we have chosen to present our arguments in a dimensional way, because we felt this to be more appropriate to present the particle-particle interaction laws on grain level. Here, the *functional* form of the interaction is still a controversial point in the literature (cf. e.g., [21]) and thus a dimensionless representation has only little additional value. However, we present here a dimensionless form of the most important equations in the text and values for the arising dimensionless groups.

If we measure lengths in the system in units of the average particle radius $\bar{r}$ and if we select the Stokes velocity V_S as the reference velocity then the natural time scale of the problem is $\bar{r}/V_S$. In the following we will use a superscript asterisk to denote dimensionless quantities. Thus, we obtain, for example,

$$\vec{u} = V_S \vec{u}^*, \quad \vec{x} = \bar{r}\vec{x}^*, \quad \text{and} \quad \frac{\partial}{\partial t} = \frac{V_S}{\bar{r}} \frac{\partial}{\partial t^*}. \tag{A1}$$

The system of Eq. (11) and Eq. (12) describing the fluid dynamics becomes, using the above notation and after division by $\epsilon V_S^2 \rho_l$,

$$\frac{\partial \vec{u}^*}{\partial t^*} + (\vec{u}^* \vec{\nabla}^*)\vec{u}^* = -\epsilon \vec{\nabla}^* p^* + \mathrm{Re}^{-1} (\vec{\nabla}^*)^2 \vec{u}^* + \vec{f}^*, \tag{A2}$$

$$\frac{\partial \epsilon}{\partial t^*} + \vec{\nabla}^* \cdot (\epsilon \vec{u}^*) = 0. \tag{A3}$$

Here, $\mathrm{Re} \equiv \bar{r}\rho_l V_S/\eta$, the dimensionless pressure $p^* \equiv p\bar{r}/V_S^2\rho_l$, and the dimensionless force density $\vec{f}^* \equiv \vec{f}\bar{r}/V_S^2\rho_l$. The force density comprises contributions from the particle-liquid momentum interchange and from the gravitation acting on the liquid. We will briefly discuss the corresponding terms close to the end of this Appendix.

We now impose on the particle interaction equations the time and length scales selected above. It is thus not surprising that we will see simplifications in these equations only where the particle-liquid interaction is concerned. Newton's third law, written for the particle velocities $\vec{v}_i \equiv \dot{\vec{x}}_i$,

$$m \frac{d}{dt} \vec{v}_i = \vec{F}_i, \tag{A4}$$

becomes

$$\mathrm{St} \frac{d}{dt^*} \vec{v}_i^* = \frac{1}{6\pi\eta\bar{r}V_S} \vec{F}_i \equiv \vec{F}_i^*. \tag{A5}$$

In this relation, the Stokes number $\mathrm{St} \equiv mV_S/6\pi\eta\bar{r}^2$ measures the importance of particle inertia as compared to viscous effects of the interaction with the surrounding liquid. We will in this Appendix for simplicity ignore the small polydispersivity of the particles in the system and assume that they are all of equal size. Let us first focus on the drag force $\vec{F}_i^d$ and the gravitational contribution $m\vec{g}$ to $\vec{F}_i$,

$$\vec{F}_i = 6\pi\eta\bar{r}(\vec{u} - \vec{v}) + m\vec{g} + \quad \text{(two-body terms)}. \tag{A6}$$

Dividing by $6\pi\eta\bar{r}V_S$ and using $V_S = mg(1-\rho_l/\rho_p)/6\pi\eta\bar{r}$ [cf. Eq. (25)], the preceding two terms simplify considerably to

$$\vec{F}_i^* = \vec{u}^* - \vec{v}^* + \vec{e}_g + \quad \text{(two-body terms)}, \tag{A7}$$

where $\vec{e}_g$ is just the unit vector in the direction of $\vec{g}$.

Since the chosen scales are not adapted to the regime where particle-particle overlap occurs, we achieve no corresponding simplification in the interparticle equations. Only the lubrication part of the equations takes a simple form. We obtain for the dimensionless normal component $\vec{F}_{ij}^{*n}$ of the interparticle force [Eq. (8)],

$$\vec{F}_{ij}^{*n} = \vec{F}_{ij}^{c*,n} + \vec{F}_{ij}^{l*,n} = \begin{cases} \vec{0}, & \text{if } (-\xi_{ij}^*) > 1/2, \\ -\frac{1}{2}\left(\dfrac{1}{-2\xi_{ij}^*+\delta} - \dfrac{1}{1+\delta}\right)[(\vec{v}_j^* - \vec{v}_i^*)\cdot\vec{n}_{ij}]\vec{n}_{ij}, & \text{if } 0 < (-\xi_{ij}^*) < 1/2, \\ [-k_n^*\xi_{ij}^* - 2\gamma_n^*(\vec{v}_j^* - \vec{v}_i^*)\cdot\vec{n}_{ij}]\vec{n}_{ij}, & \text{if } \xi_{ij}^* > 0. \end{cases} \tag{A8}$$

Here, we have defined the dimensionless spring constant,

$$k_n^* \equiv \frac{k_n}{6\pi\eta V_S} = \frac{k_n\bar{r}}{m(1-\rho_l/\rho_p)g}, \tag{A9}$$

which measures the strength of the restoring force between two particles in comparison to the gravitational force corrected by buoyancy, and the dimensionless damping

$$\gamma_n^* \equiv \frac{\gamma_n m_{\mathrm{red}}}{6\pi\eta\bar{r}} = \frac{1}{4}\left(\frac{1}{\delta} - \frac{1}{1+\delta}\right). \tag{A10}$$

In the last step we have made use of the value of γ_n given in Eq. (7). The equations for the tangential component of the particle contact forces (10) introduce two additional parameters:

$$\vec{F}_{ij}^{*t} = -\min(\mu|\vec{F}_i^{*n}|, 2\gamma_t^*|\vec{v}_{ij}^{*t}|)\frac{\vec{v}_{ij}^{*t}}{|\vec{v}_{ij}^{*t}|}. \tag{A11}$$

Here, we define the dimensionless tangential damping coefficient $\gamma_t^* \equiv \frac{\gamma_t m_{\mathrm{red}}}{6\pi\eta\bar{r}}$, whereas the Coulomb friction coefficient is already dimensionless.

The remaining task is to find the expression for the volume force term in the Navier-Stokes equation (A2). It comprises a gravitational contribution $\rho_l\vec{g}$ and a local average of the drag forces acting between liquid and particles. We write

$$\vec{f}^* \equiv \vec{f}\bar{r}/V_S^2\rho_l = \frac{\bar{r}}{\rho_l V_S^2}\frac{1}{\epsilon V}\sum_V \vec{F}_i^d + \frac{\bar{r}g}{V_S^2}\vec{e}_g, \tag{A12}$$

where the sum $\sum_V$ extends over the particles within an averaging cell with volume V. We choose $V = (\Delta x)^2 z$, corresponding to the volume associated with one grid point. We use relations (A6) and (A7) to find

$$\vec{f}^* = \frac{6\pi}{\mathrm{Re}}\frac{1}{\epsilon}\left(\frac{a}{\Delta x}\right)^2\frac{a}{z}\sum_V(\vec{v}_i^* - \vec{u}^*) + \mathrm{Fr}\,\vec{e}_g. \tag{A13}$$

where the liquid velocity is understood to be interpolated to the particle location, in the spirit explained in Sec. II C. The dependence of the friction force on the inverse Reynolds number is typical for the low-Reynolds-number regime. The gravitational influence on the liquid is measured by a particle-size-based Froude number $\mathrm{Fr} \equiv \bar{r}g/V_S^2$.

In the case of flow through a random medium, $\mathrm{Fr} = 0$ and the velocity scale is set by the superficial fluid velocity instead of the Stokes velocity V_S — the dimensionless formulation can then be obtained by substituting the superficial fluid velocity wherever V_S occurred in the expressions above. Of course, the parameters characterizing interparticle interactions are of no importance in this case.

Apart from the nondimensional parameters so far, there are quantities characteristic of the geometry of the problem that do not explicitly occur in the equations of motion shown above. These are the ratio of system width to average particle radius, $L_x/\bar{r}$ and the aspect ratio of the simulation volume L_x/L_y. Two more parameters are the ratio of the reference length z to the particle radius $z/\bar{r}$, the ratio of the grid spacing to the particle radius, $\Delta x/\bar{r}$. These are of numerical nature, but specify as well the averaging volume for the drag-force feedback. The particle density in the system is specified by the average volume fraction $\bar{\epsilon}$.

For the two sets of simulations that we have performed the corresponding dimensionless parameters are listed in Tables I and II.

[1] J. Happel and H. Brenner, *Low Reynolds Number Hydrodynamics* (Prentice Hall, Englewood Cliffs, NJ, 1965).
[2] S. L. Soo, *Fluid Dynamics of Multiphase Flow* (Blaisdell, Waltham, MA, Toronto, 1967).
[3] J. Feng, H. H. Hu, and D. D. Joseph, J. Fluid Mech. **261**, 95 (1994).
[4] A. Ladd, J. Fluid Mech. **271**, 311 (1994).
[5] J. F. Brady and G. Bossis, Ann. Rev. Fluid Mech. **20**, 111 (1988).
[6] B. Cichocki, B. U. Felderhof, K. Hinsen, E. Wajnryb, and J. Blawzdziewicz, J. Chem. Phys. **100**, 3780 (1994).
[7] A. J. C. Ladd, J. Chem. Phys. **88**, 5051 (1988).
[8] F. R. da Cunha, Ph.D. thesis, University of Cambridge, Robinson College, 1995.
[9] K. Ichiki and H. Hayakawa, Int. J. Mod. Phys. B **7**, 1899 (1993).
[10] A. L. Fogelson and C. S. Peskin, J. Comput. Phys. **79**, 50 (1988).
[11] R. Jackson, in *Fluidization*, edited by D. Harrison, J. F. Davidson, and R. Clift (Academic, London, 1985).
[12] G. K. Batchelor, J. Fluid Mech. **193**, 75 (1988).
[13] P. A. Cundall and O. D. Strack, Geotechnique **29**, 47 (1979).
[14] M. P. Allen and D. J. Tildesley, *Computer Simulations of Liquids* (Clarendon Press, Oxford, 1987).
[15] Y. Tsuji, T. Tanaka, and T. Ishida, Powder Technol. **71**, 239 (1992).
[16] S. Yonemura, T. Tanaka, and Y. Tsuji, ASME/FED **166**, 303 (1993).
[17] R. E. Caflisch and J. H. Luke, Phys. Fluids **28**, 759 (1985).
[18] E. J. Hinch, in *Disorder and Mixing*, edited by E. Guyon, J.-P. Nadal, and Y. Pomeau (Kluwer Academic, Dordrecht, 1988), p. 153.
[19] D. L. Koch and E. Shaqfeh, J. Fluid Mech. **224**, 275 (1991).
[20] A. J. Goldman, R. G. Cox, and H. Brenner, Chem. Eng. Sci. **22**, 637 (1967).
[21] O. R. Walton, in *Particulate Two-Phase Flow*, edited by M. C. Roco (Butterworth-Heinemann, Boston, 1992), Chap. 25.
[22] G. Ristow, Ann. Rev. Comput. Phys. **1**, 275 (1995).
[23] R. H. Davis, in *Mobile Particulate Systems*, edited by E. Guazzelli and L. Oger (Kluwer Academic Publishers, Dordrecht, 1995).
[24] A. J. Chorin, J. Comput. Phys. **2**, 12 (1967).
[25] A. J. Chorin, J. Math. Comput. **22**, 745 (1968).
[26] R. Peyret and T. D. Taylor, *Computational Methods for Fluid Flow*, Springer Series in Computational Physics (Springer, New York, 1983).
[27] S. V. Patankar, *Numerical Heat Transfer and Fluid Flow* (Hemisphere Publishing Corporation, New York, 1980).
[28] H. Kopetsch, *20. IFF Ferienkurs: Computersimulationen in der Physik* (KFA Jülich, Jülich, 1989).
[29] B. E. Launder and D. B. Spalding, *Mathematical Models of Turbulence* (Academic, London, 1972).
[30] M. R. Maxey and J. J. Riley, Phys. Fluids **26**, 883 (1983).
[31] S. Ergun and A. A. Orning, Ind. Eng. Chem. **41**, 1179 (1949).
[32] S. Ergun, Chem. Eng. Prog. **48**, 89 (1952).
[33] L. D. Landau and E. M. Lifshitz, *Mécanique des Fluides*, 2nd ed. (Mir Publishers, Moscow, 1989).
[34] F. A. L. Dullien, *Porous Media: Fluid Transport and Pore Structure* (Academic, New York, 1979).
[35] H. C. Brinkman, Appl. Sci. Res. A **1**, 27 (1947).
[36] S. Childress, J. Chem. Phys. **56**, 2527 (1972).
[37] H. Nicolai, B. Herzhaft, E. J. Hinch, L. Oger, and E. Guazelli, Phys. Fluids **7**, 12 (1995).
[38] J.-Z. Xue, E. Herbolzheimer, M. A. Rutgers, W. B. Russel, and P. M. Chaikin, Phys. Rev. Lett. **69**, 1715 (1992).
[39] J. F. Richardson and W. N. Zaki, Trans. Inst. Chem. Eng. **32**, 35 (1954).
[40] A. Ladd, J. Fluid Mech. **271**, 285 (1994).
[41] G. K. Batchelor and J. T. Green, J. Fluid Mech. **56**, 375 (1972).
[42] F. Feuillebois, J. Fluid Mech. **139**, 145 (1984).
[43] I. Goldhirsch and G. Zanetti, Phys. Rev. Lett. **70**, 1619 (1993).
[44] S. McNamara and W. R. Young, Phys. Fluids A **5**, 34 (1993).
[45] E. J. Hinch, J. Fluid Mech. **83**, 695 (1977).
[46] H. Nicolai and E. Guazelli, Phys. Fluids **7**, 3 (1995).
[47] W. Kalthoff, S. Schwarzer, G. Ristow, and H. Herrmann, Report No. cond-mat 9501128.